

Supplementary Materials for

Ultrafast dissolution and creation of bonds in IrTe₂ induced by photodoping

Shin-ichiro Ideta, Dongfang Zhang, Arend G. Dijkstra, Sergey Artyukhin, Sercan Keskin, Roberto Cingolani, Takahiro Shimojima, Kyoko Ishizaka, Hiroyuki Ishii, Kazutaka Kudo, Minoru Nohara, R. J. Dwayne Miller*

*Corresponding author. Email: dwayne.miller@mpsd.mpg.de

Published 27 July 2018, *Sci. Adv.* **4**, eaar3867 (2018)
DOI: 10.1126/sciadv.aar3867

This PDF file includes:

Section S1. Experimental methods
Section S2. Sample preparation
Section S3. Diffraction pattern of IrTe₂
Section S4. Dynamics on the Bragg and superlattice peaks
Section S5. Thickness dependence of lattice dynamics for Bragg and superlattice peaks
Section S6. Power dependence of lattice and electron dynamics
Section S7. DFT calculations
Section S8. Lattice temperature increases with the fluence of pump pulse
Fig. S1. Schematic diagram of the FED setup.
Fig. S2. Thin films and the TEM image.
Fig. S3. Delay time dependence of diffraction pattern.
Fig. S4. Lattice dynamics obtained from several BPs and SLs.
Fig. S5. Relative diffraction intensity change of IrTe₂ with different film thicknesses of 20 to 100 nm.
Fig. S6. Fluence dependence of FED and optical pump-probe experiments.
Fig. S7. Difference of electronic free energies of dimerized and HT structures as a function of electronic temperature, as calculated using DFT.
Fig. S8. Calculated forces on Ir ions after optical excitation.
Fig. S9. Calculated forces on the Ir ions in the dimerized structure after an instantaneous optical excitation.
Fig. S10. DOS contributions from the Ir ions.
References (30–32)

Section S1. Experimental methods

Time-resolved diffraction measurements were carried out in the transmission mode at a repetition rate of 1 kHz, corresponding to 1 millisecond, to minimize the effects of surface charging, suppression of thermal heating, and temporal spatial mismatch (24). The schematic illustration of the compact DC-accelerated electron diffraction setup. A part of the fundamental (800 nm, 50 fs) output beam from a commercial Ti:sapphire laser system (Coherent) was split into two arms by a beam splitter. Infrared optical pulses were converted to 266 nm through the third harmonic generation nonlinear processes. The 266-nm probe was directed onto a gold photocathode generating ultrashort electron pulses. Photoelectrons were finally accelerated to 128 kV by a DC electric field between the photocathode and anode plates. Diffracted and directly transmitted electrons were focused with the magnetic lens onto a 1:1 fiber-coupled CCD camera (Quad-RO 4320, Princeton Instruments) coated with a P20 phosphor scintillator. The optical time delay between the photoexcitation and electron pulses was adjusted by changing the optical pump-probe path difference using a motorized translational stage. Photoinduced structural changes were initiated by 800 and 400 nm pump pulses focused (full width at half maximum, FWHM) on the sample. Taking the duration of the optical pump pulse into account, the overall instrumental time resolution was 240 - 290 fs (FWHM). Optical pump-probe experiments were performed in reflection mode on single-crystalline IrTe₂ at room temperature and ~ 200 K in the vacuum chamber (~ 10⁻⁶ Pa). All samples were photoexcited with 400 nm (3.1 eV) and 800 nm (1.55 eV) optical pump pulses focused on the target at an incident angle of 10 degrees from the surface normal. The probe was focused within the photoexcited area of the sample. The reflected signal intensities were registered with a slow photodiode (~100 ms response time).

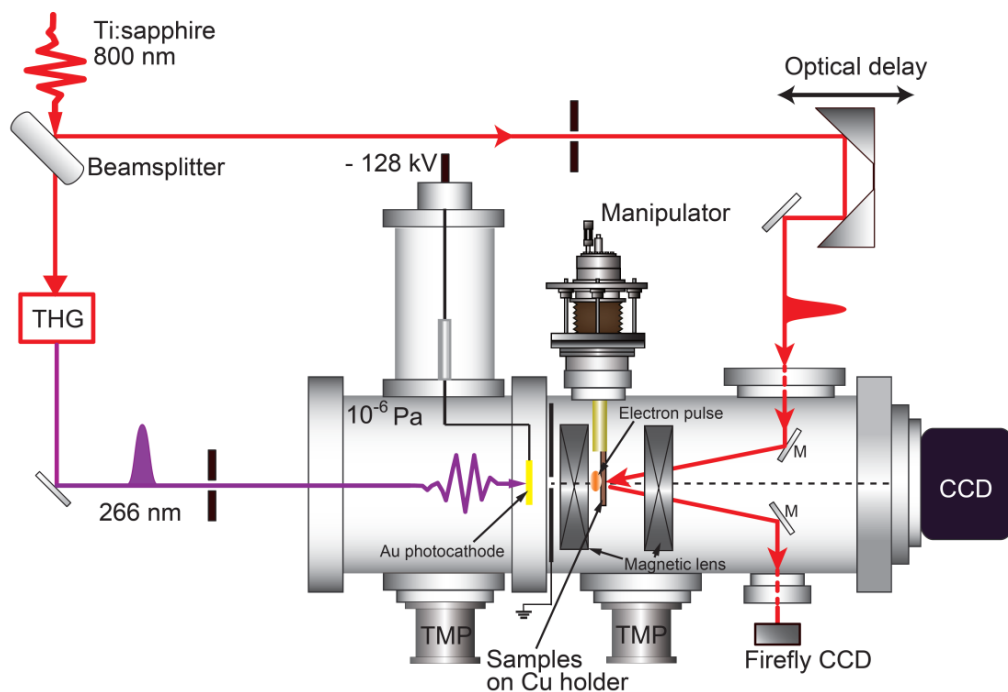


Fig. S1. Schematic diagram of the FED setup. TMP, turbo molecular pump; CCD, charge-coupled device camera; THG, third harmonic generation.

Section S2. Sample preparation

Transition-metal dichalcogenide IrTe_2 undergoes a structural phase transition from trigonal phase to complex triclinic phase at temperature of 260 K (7). IrTe_2 single crystals were cleaved between IrTe_6 octahedra-slab planes using an ultramicrotome diamond knife to obtain 20, 30, 40, 60, 80, and 100 nm thick, $\sim 150 \times 100 \mu\text{m}^2$ free standing crystals (sheets). The samples were picked up from the water surface using the host copper grid (see fig. S2). The grid was clamped to the sample holder ensuring good thermal contact.

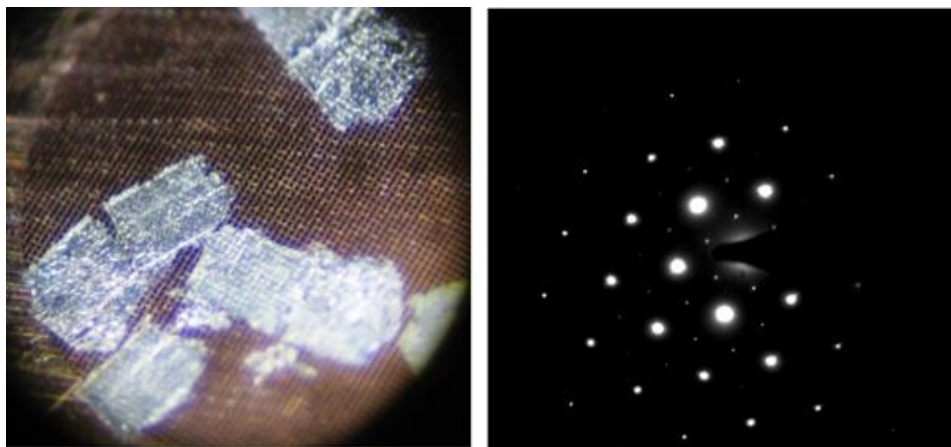


Fig. S2. Thin films and the TEM image. Several 20 nm thick IrTe_2 crystals on the copper grid (left) and transmission electron microscopy image taken at 80 kV-electron beam at room temperature (right).

Section S3. Diffraction pattern of IrTe_2

Comparison with relative intensity changes of diffraction patterns. We found that Bragg and nearest neighboring superlattice peaks are observed clearly in the normal experimental geometry and the other superlattice peaks are observed in the geometry with the sample by the tilt of 10 degrees compared with the normal position against the direction of electron pulses. All of the superlattice peaks show similar dynamics as a function of delay time.

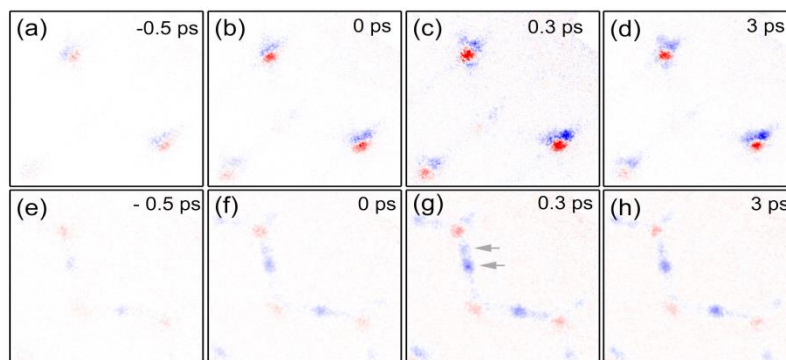


Fig. S3. Delay time dependence of diffraction pattern. (a to d), Diffraction images taken by electron pulses to probe the dynamics perpendicular to the sample surface. (e to h), Same set of (a to d), but with the sample tilted by 10 degrees relative to the electron pulses propagation direction. These are differential images in which the pump-probe images are subtracted from the probe only image. Red and blue color corresponds to the increase and decrease of the diffraction intensity, respectively.

Section S4. Dynamics on the Bragg and superlattice peaks

We analyzed the other Bragg (BP) and superlattice (SL) peaks and confirmed that the trend of dynamics was almost the same. We analyzed eight BP and SL peaks which are showing reasonable signal to noise ratio in the present study as shown below. Difference of the relative intensity obtained from BP and SL indicates symmetry breaking.

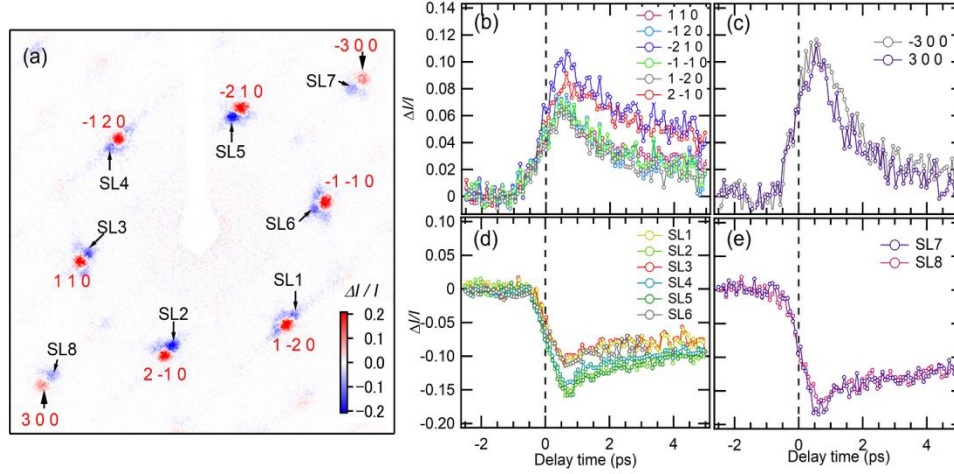


Fig. S4. Lattice dynamics obtained from several BPs and SLs. (a) Evolution of Bragg and superlattice intensities illustrated as relative change at 0.6 ps after photoexcitation. (b) to e) Corresponding dynamics of $\Delta I_{\text{Bragg}}/I_{\text{Bragg}}$ and $\Delta I_{\text{SL}}/I_{\text{SL}}$ at several peak positions.

Section S5. Thickness dependence of lattice dynamics for Bragg and superlattice peaks

We observe thickness dependence of the lattice dynamics of IrTe₂ with 20 to 100 nm thickness. The result is summarized in fig. S5. The fluence was set at $\sim 0.55 \text{ mJ/cm}^2$ to keep the peak power in the linear excitation regime and $T \sim 200 \text{ K}$. Lattice dynamics are strongly dependent on the sample thickness: the photoinduced change are clearly observed for 20, 30, and 40 nm thick samples, on the other hand, the samples of 50 nm and thicker do not show clear change for both Bragg and superlattice peaks even with much higher fluence. The relative intensity change $\Delta I/I$ was estimated from the maximum and minimum of Bragg and superlattice peaks, respectively, in fig. S5. Studies reported in Fig. 2 were performed for samples with thickness in the 20-40 nm range. We attribute this effect to reduced valence excitation for the fixed excitation condition at the thickest crystals because the penetration depth of the pump laser in metals is normally in the range of a few tens of nm and multiple scattering effect masking the underlying cooperative lattice dynamics.

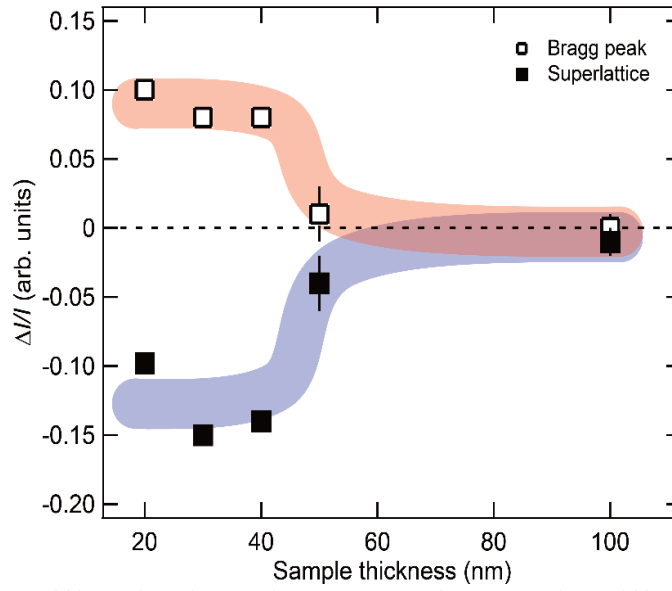


Fig. S5. Relative diffraction intensity change of IrTe₂ with different film thicknesses of 20 to 100 nm. The maximum photoinduced $\Delta I/I$ is plotted as a function of sample thickness. Translucent blue and red curves shown as the guide for the eye.

Section S6. Power dependence of lattice and electron dynamics

Figure S6(a) shows the fluence dependence of diffraction change for Bragg and superlattice peak at the optical delay time ~ 1 ps for a sample 40 nm thick. $\Delta I/I_0$ displays an almost linear dependence. One can see that the obvious oscillation corresponding to an optical coherent phonon is observed as shown in figs. S6(b)-S6(e) in going from low to high fluence. At the HT phase, relaxation and rise time constants are estimated by single and double exponential fitting with $\tau = 0.25 \pm 0.05$ and $t_r \sim 0.15$ ps, respectively, and that at the LT phase shows the same time constant. There is a large transient which decays back to the initial value with a long time constant that strongly depends on fluence in the LT phase. Although the oscillation can be observed in the high fluence at LT phase, the oscillation period remains constant as shown in fig. S6(e). With increasing the fluence, the amplitudes of oscillation increase up to the fluence performed in the present study and do not disappear. It is noteworthy that in 40 nm thickness sample, we also noticed that while increasing the fluence that can bring the whole material into the HT phase. However, the recovery time is much longer than the laser repetition rate. Only at low excitation level, bond breaking can happen that the structure can recover within a short time.

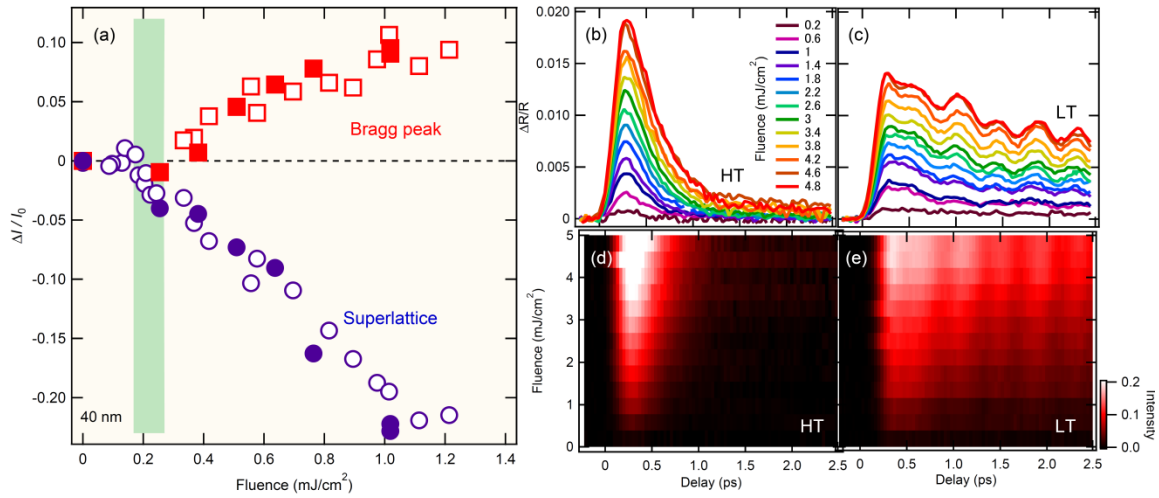


Fig. S6. Fluence dependence of FED and optical pump-probe experiments. (a) Relative intensity change for Bragg and superlattice peaks at ~ 1 ps for 40 nm thick sample after photoexcitation is plotted as a function of fluence. Filled and unfilled symbols reflect 400 and 800 nm pump, respectively. Fluence dependence of time-resolved optical reflectivity measurement at room temperature and ~ 200 K is shown in (b) and (c), and these results are shown by intensity plot in (d) and (e), respectively. In the low temperature, the oscillations correspond to coherently excited optical phonons.

Section S7. DFT calculations

To study the effect of optical excitation on the structural dynamics of IrTe_2 DFT simulations were performed using the projector augmented wave formalism for core-valence partitioning as implemented in the Quantum Espresso code (29). $6s$, $6p$, and $5d$ states of Ir and $5s$, $5d$, and $4p$ states of Te were included in the valence. The PBEsol functional was used, as it was demonstrated to stabilize the dimerized state (30). Electron-electron interactions in metals lead to fast relaxation of electrons in the conduction band after photo-excitation, therefore we assumed that the electronic excited state on the lattice timescale could be modeled by a thermal equilibrium with an effective electronic temperature. This temperature was enforced by smearing the occupations of electronic states using a Fermi-Dirac distribution. We can describe it with a Fermi-Dirac distribution with a certain elevated temperature from ambient, which is a good approximation if electron-electron scattering is fast enough.

We calculated the total energy of the Ir-Ir 1/5 dimerized state (see Fig. 4 in the main text, fig. S7), experimentally observed below 260 K, and the non-dimerized state, which is stable at room temperature, for various values of the electronic temperature. For low electronic temperature, we found that the dimerized state has the lowest total energy. When the electronic temperature exceeds 0.02 Ry (~ 0.27 eV), the situation is reversed, and we find that the non-dimerized state has a lower total energy than the dimerized one. This means that the dimers will break given sufficient time. Surprisingly, we found that the dimerized state becomes stable again when the electronic temperature exceeds 0.1 Ry (~ 1.36 eV). Thus, we find that the Ir-Ir dimerized state is stable for low and for high electron temperature while the dimers break for intermediate electron temperatures (fig. S7). While the results presented here were obtained from density functional theory calculations using the fixed experimental crystal structures, we repeated our calculations by relaxing the experimental structures at a given electronic temperature and found the

same trend. We also performed calculations with and without spin-orbit coupling included. The spin-orbit coupling leads to destabilization of the dimerized phase at a lower electronic temperature; at electronic temperatures well above the spin-orbit coupling scale, the energy difference between the two phases is unaffected by it.

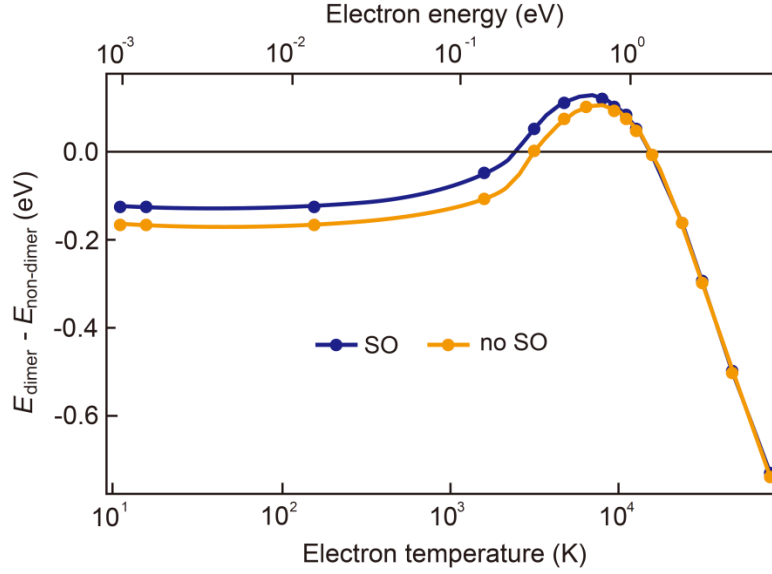


Fig. S7. Difference of electronic free energies of dimerized and HT structures as a function of electronic temperature, as calculated using DFT. The continuous curves are guides to the eye. ‘SO’ refers to calculations where spin-orbit coupling was taken into account using relativistic PAW datasets (31) and PBEsol exchange-correlation functional while ‘no SO’ are the data presented in Figure 3 in the main text, generated with spin orbit coupling being neglected.

Forces were calculated by fixing occupations of bands after exciting an electron from the valence band to the conduction band. For the 0.98 eV excitation energy mentioned in the main text, the occupations of bands around the Fermi level were ..., 2.0, 1.0, 1.0, 0.0, 0.52, 0.47, ..., in order of increasing energy.

In the random phase approximation (RPA) the absorption coefficient is given by

$$\alpha(\omega) \sim \sum_{i,f} \frac{|<i|p|f>|^2 n_i(1-n_f)}{\varepsilon_i - \varepsilon_f + \hbar\omega}, \text{ where } i \text{ and } f \text{ denote the initial and final states, respectively,}$$

n_i and n_f are their occupations and ε_i and ε_f their energies. Here the matrix elements of the momentum operator p are non-zero between the states with opposite parity and determine the selection rules for dipole-allowed transitions. If one neglects the matrix elements, one gets the joint density of states, that has peaks at ω for each pair of occupied and empty bands, separated by $\hbar\omega$. In particular, there is a prominent peak coming from the transitions from the bonding to antibonding bands. To simulate the effect on the structure due to absorption at frequency ω , leading to excitation involving these orbitals, we started from the unperturbed ground state band structure, $n_0(\nu, k) = 2f(\varepsilon_{\nu,k} - \mu)$, with the Fermi-Dirac function, $f(\varepsilon) = 1/(e^{\varepsilon/kT} + 1)$ with $kT \ll \mu$, μ the Fermi energy and $\varepsilon_{\nu,k}$ the energy of band ν at k -point k . We added the excitation $n_e(\nu, k) = A(-c_1\delta(\varepsilon - \varepsilon_1) + c_2\delta(\varepsilon - \varepsilon_2))$, where $\delta(\varepsilon)$ is a narrow Gaussian (0.1 eV wide) centered at energy ε ; c_1, c_2 were chosen so that the total number of electrons was conserved, $\sum_{\nu,k} n_e(\nu, k) = 0$ and a total of one electron was excited. The cutoff function $A(n > 2) = 2, A(0 < n < 2) = n, A(n < 0) = 0$ ($n = n_0 + n_e$) ensures that occupations do not exceed 2 or fall below zero. Within the

limitations of the software used, we set constant occupations throughout the Brillouin zone, and determined $n_0(v,k)$ from the band energies at a single k-point obtained after relaxing the dimerized structure on a 4x4x2 k-point grid. This procedure led to the occupations given above. From the calculated forces shown in Fig. 3B of the main text, we can see that after optical excitation the ions start moving towards the non-dimerized structure. Large forces on the two dimerized Ir ions are directed in a way that they break the dimers. Furthermore, as is demonstrated in figs. S8 (a) and (b), the forces on the two dimerized Ir ions are directed in such a way that they will lead to breaking of the dimer for excitation energies of 0.61 and 0.98 eV. On the other hand, those ions move in the opposite direction when the excitation energy is 1.52 eV, as shown in fig. S8(c). Figure S9 indicates that the three-dimensional forces of Ir ions in the dimerized state with the same conditions of fig. S8. Major contribution to the density of states (DOS) for these bands is coming from d orbitals of the dimerized Ir-Ir ions (fig. S10). This confirms the scenario in which the d_{xy} antibonding orbital plays a key role in the ultrafast melting of the dimers.

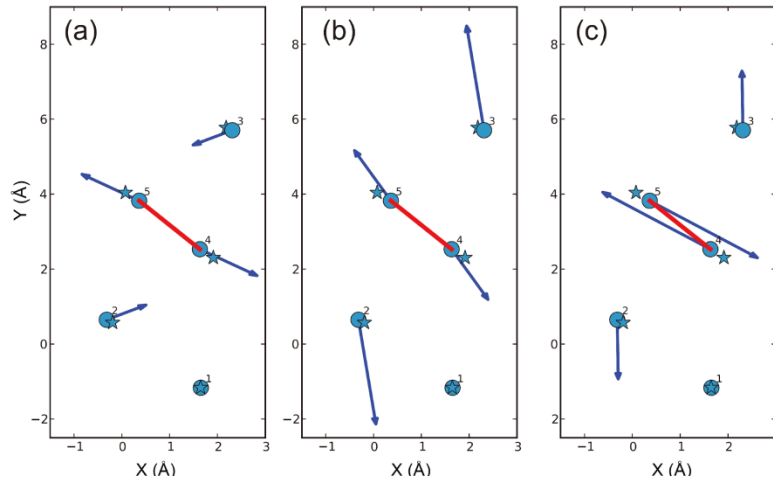


Fig. S8. Calculated forces on the Ir ions after optical excitation. Calculated forces on the Ir ions in the dimerized structure with different optical excitation (a) 0.61 eV, (b) 0.98 eV, (c) 1.52 eV in the X and Y directions. The Ir ions of the dimerized structure are shown by circles, the undimerized structure by stars. The dimerized structure and the forces are shown by a red line and blue arrows, respectively.

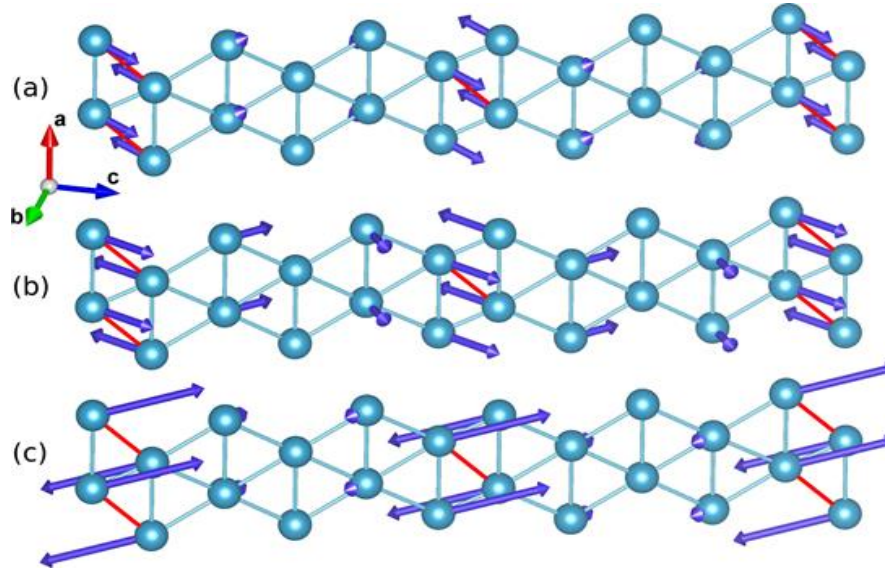


Fig. S9. Calculated forces on the Ir ions in the dimerized structure after an instantaneous optical excitation with an energy. (a) 0.61 eV, (b) 0.98 eV, (c) 1.52 eV. A total of 1 electron per 15 ion supercell is transferred to the upper bands by the excitation. A single triangular Ir layer is shown, with cyan balls representing the Ir ions, while the Te ions are hidden for clarity. The short bonds within the dimers are highlighted in red. The arrows indicating the forces are scaled so that the magnitude of the force on the dimerized Ir in panel (a) is 0.26 eV/Å.

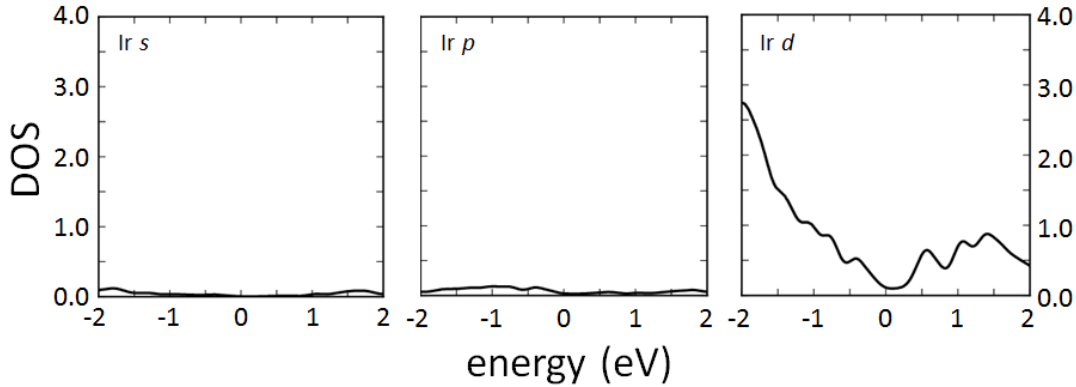


Fig. S10. DOS contributions from the Ir ions. Only the contribution of the charge inside the PAW spheres is shown.

Section S8. Lattice temperature increases with the fluence of pump pulse

Relative intensity changes of 10 – 20% corresponding to the increase of lattice temperature is ~10-20 K estimated from, $\Delta T = \frac{A_{eff} \cdot F}{\rho \cdot c \cdot d_c}$, where A_{eff} is the effective absorbed incident fluence fraction across the crystal's thickness (20%), d_c the sample thickness (40 nm), ρ (9 g/cm³) the material's density, C (60 mJ/mol*K at 200 K (32)) specific heat, and an incident fluence F of 0.55 mJ/cm². This corresponds to the excitation level of around 5% of the unit cell absorbs 1 photon with 1.55 eV.